Supporting Information

Sn-mediated topological transformation of Archimedean polyhedron of Prussian-blue analogous boosts the electrocatalytic performance for alkaline hydrogen production

Yuzhu Hu,[a] Yongqiang Feng,*[a] Weihang Feng,[a] Junsheng Chen,[a] Hai Wang,[a] Tianmi Luo,[a] Chengke Yuan,[a] Liyun Cao,[a] Jianfeng Huang,[a] Xing Lu,*[b]

[a] School of Materials Science and Engineering, Shaanxi Key Laboratory of Green Preparation and Functionalization for Inorganic Materials, Key Laboratory of Auxiliary Chemistry and Technology for Chemical Industry, Ministry of Education, Shaanxi University of Science and Technology, Xi'an 710021, China. E-mail address: fengyq@sust.edu.cn

[b] State Key Laboratory of Materials Processing and Die & Mould Technology, School of Materials Science and Engineering, Huazhong University of Science and Technology, Wuhan, 430074, People's Republic of China. E-mail address: lux@hust.edu.cn

* Correspondence: fengyq@sust.edu.cn

Content

Additional Figures and Tables

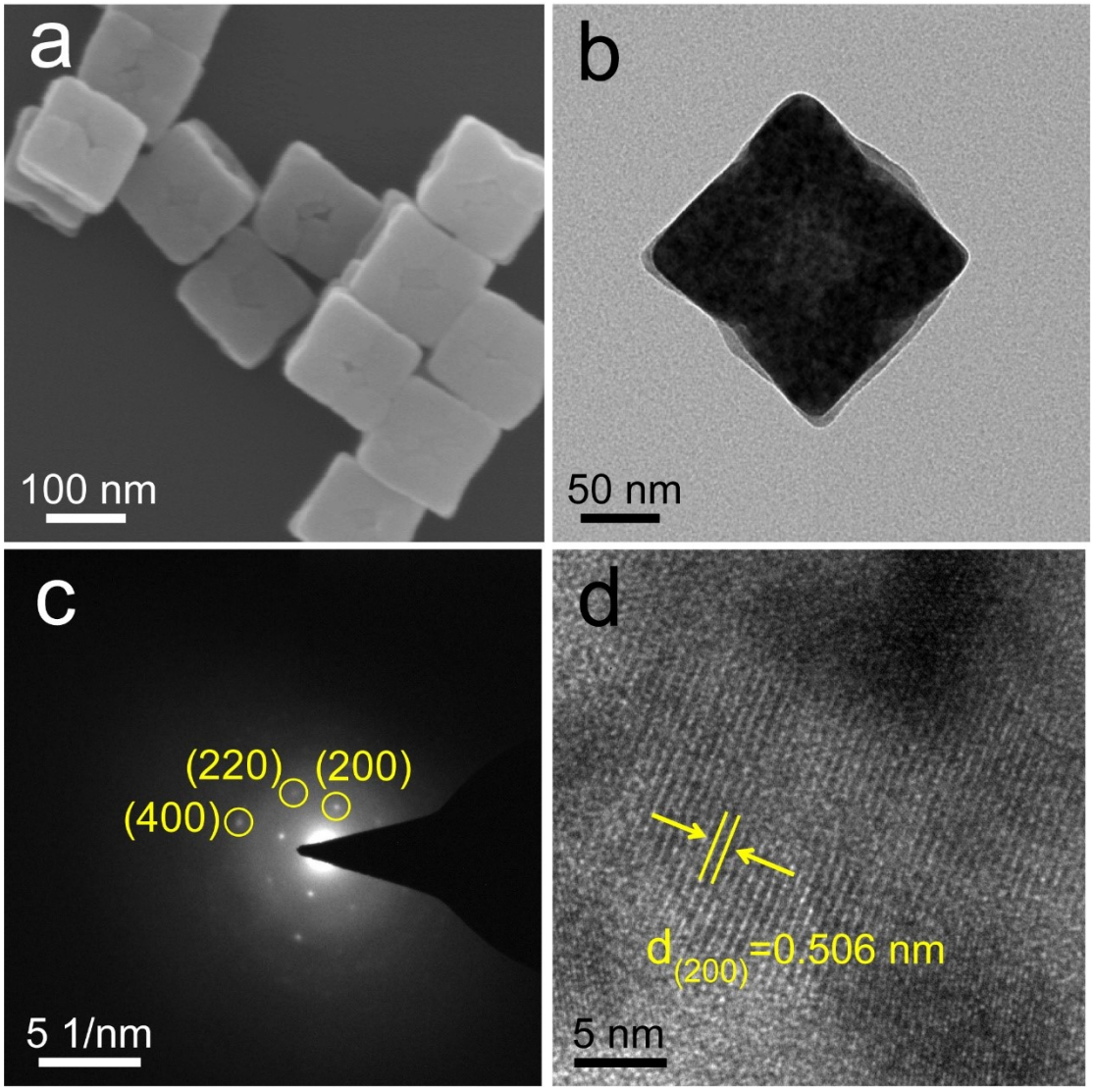

Fig. S1. (a) SEM, (b) TEM, (c) SAED and (d) HRTEM images of the CoFe PBA.

As shown in scanning electron microscopy (SEM) (Fig. S1a) and transmission electron microscopy (TEM) (Fig. S1b) images, the CoFe PBA possesses a smooth uniform solid nanocube structure with a particle size of average 150 nm. The selected area electron diffraction (SAED) pattern (Fig. S1c) exhibits discrete spots indexed to the (200), (220), and (400) planes and verifies the crystalline nature of CoFe PBA, accordance with the results observed by Shi.[1] High resolution TEM (HRTEM) image

(Fig. S1d) shows that the clear crystal lattice fringes of CoFe PBA, corresponding to an interplanar crystal spacing of 0.506 nm denotes the (200) planes.

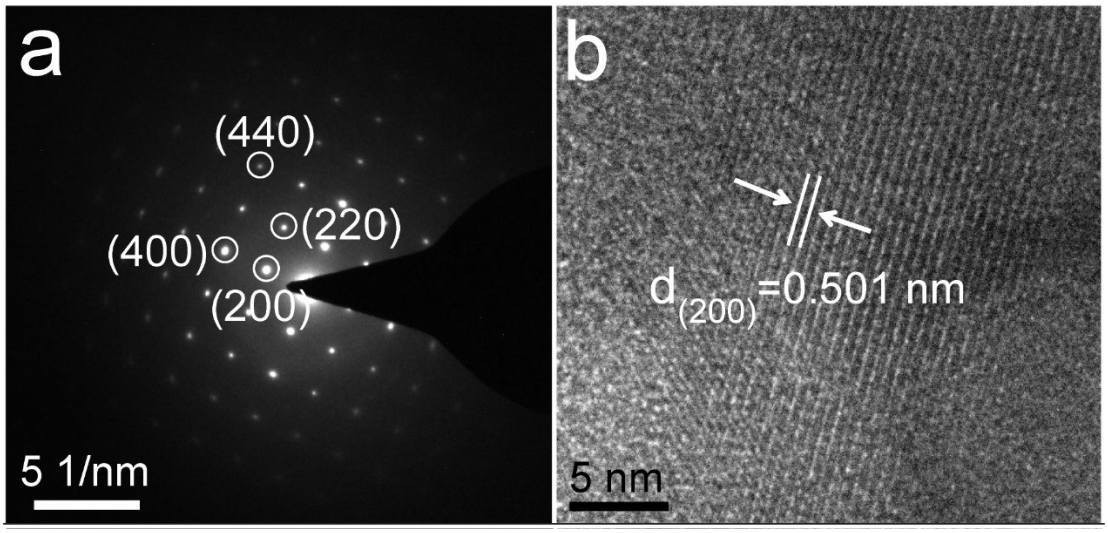

Fig. S2. (a) SAED and (b) HRTEM images of the Sn-CoFe PBA.

Remarkably, the high single crystallinity of Sn-CoFe PBA was further identified by using SAED analysis (Fig. S2a), indexed to (200), (220), (400) and (440) planes, implying a better crystallinity. Additionally, HRTEM images obtained from Fig. S2b illustrated a crystal lattice fringe spacing of Sn-CoFe PBA with 0.501 nm corresponding to the (200) plane, smaller than CoFe PBA with 0.506 nm (Fig. S1d) because of Sn insertion successfully.

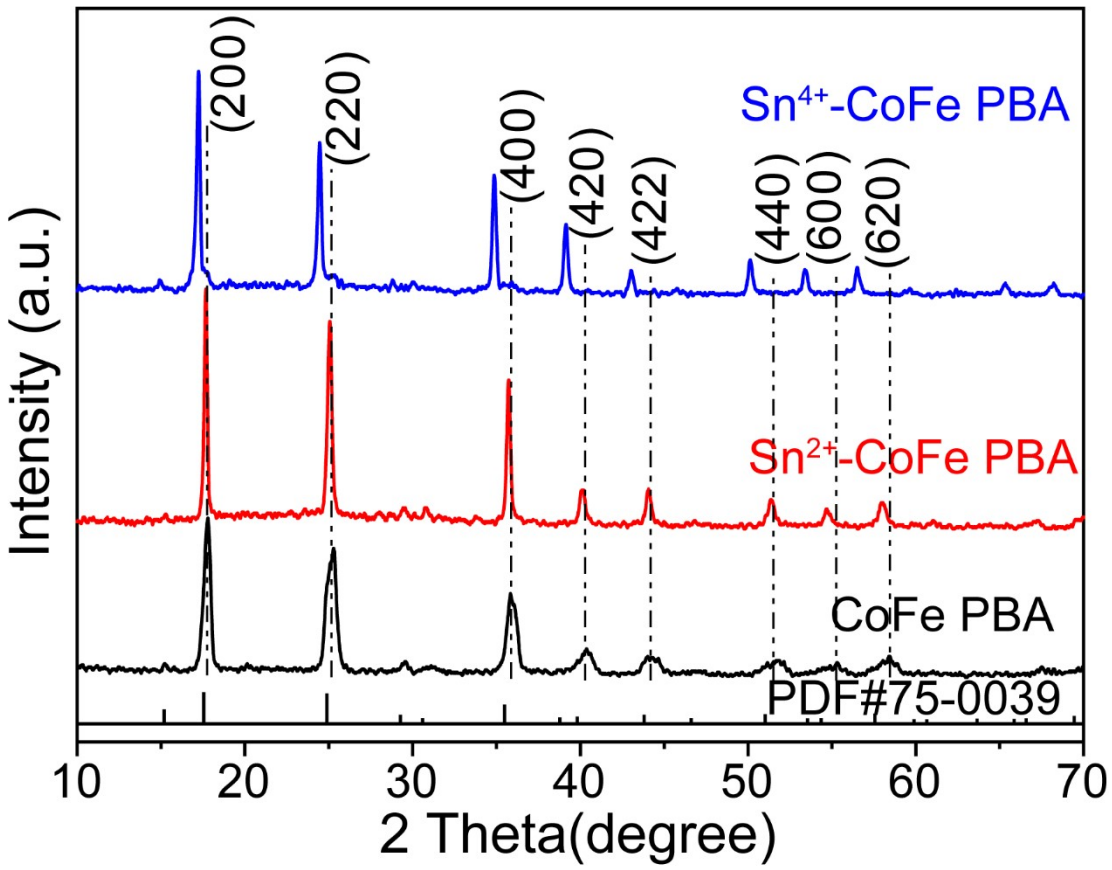

Fig. S3. XRD patterns of CoFe PBA (black), Sn^{2+}-CoFe PBA (red), Sn^{4+}-CoFe PBA (blue), respectively.

Phase compositions and crystallinities are analyzed by X-ray diffraction (XRD) spectrum. As depicted in Fig S3, all the sharp diffraction peaks can be well associated with $Co_2Fe(CN)_6$ (PDF card No. 75-0039), revealing to a great crystallinity of the substances. There is no obvious difference in material structure of the Sn-CoFe PBA compared with those of the pure CoFe PBA. However, the peak width of Sn-CoFe PBA is narrower and present a down shift after Sn^{2+} or Sn^{4+} doping, declaring increased grain sizes.

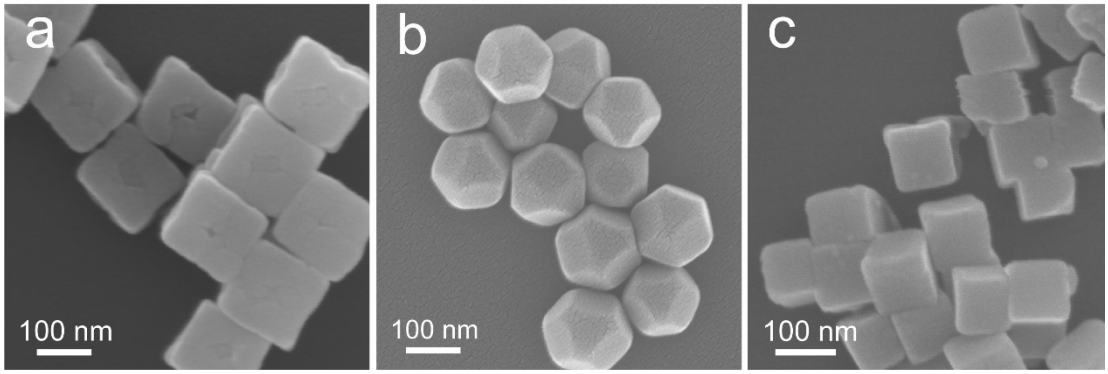

Fig. S4. SEM of (a) CoFe PBA, (b) Sn^{2+}-CoFe PBA and (c) Sn^{4+}-CoFe PBA with a molar ratio of Co^{2+}/Sn^{2+}=2:1.

Moreover, we explored the optimal molar ratio of Co^{2+}/Sn^{2+}=2:1 for Sn with different valence states by changing Sn source. The result indicated that when Sn^{4+} (0.69 Å) was used, it still maintained the shape of cube. It may be attributed to different ionic radius of Sn^{4+} and Sn^{2+}. In terms of ionic radius, the radius of Sn^{2+} have great distinction with cobalt ions and iron ions, bringing about structure transformation from cube to corner cutting polyhedron as Figs. S4a and S4b. On the contrary, the radius of Sn^{4+} is similar to other ions in Sn-CoFe PBA and Sn^{4+} stabilizes intrinsically, so it just replaces the positions of the other atoms in the lattice, not causing any structural changes. After Sn^{4+} doped, the cubes still retained its original cube structure.

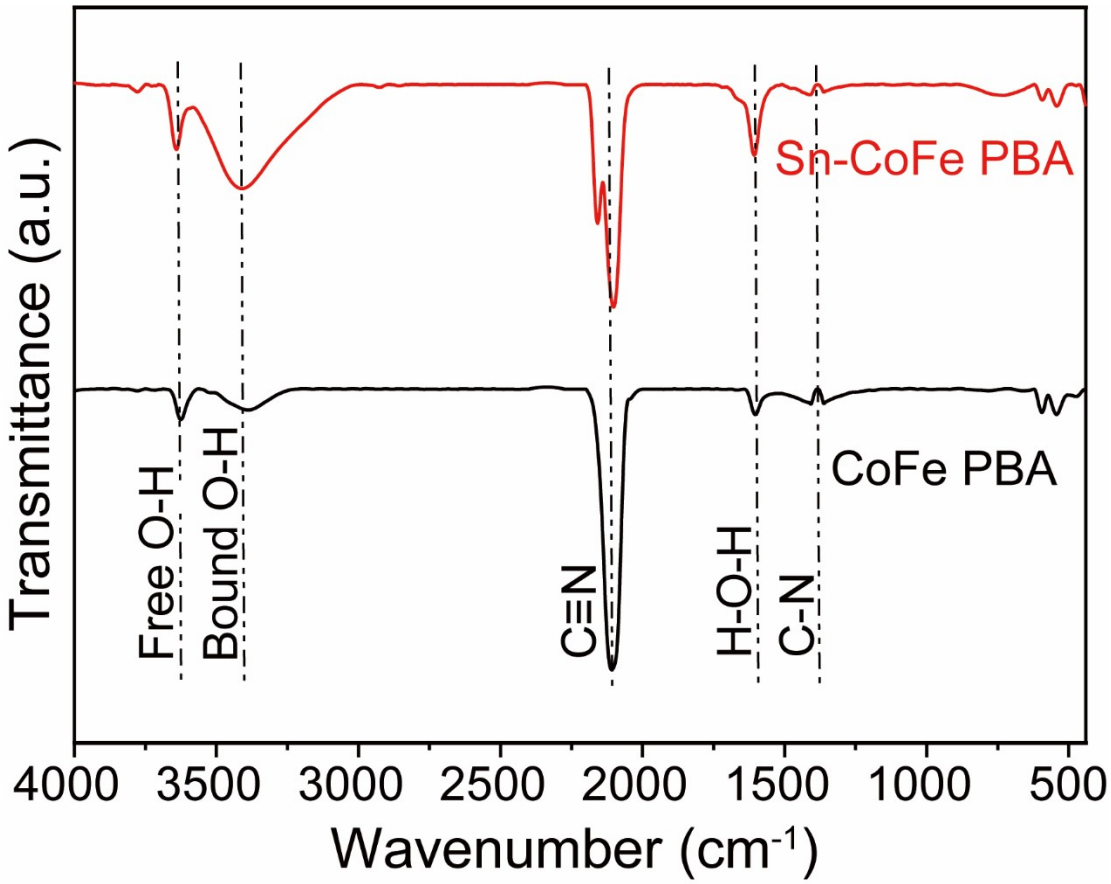

Fig. S5. FTIR spectra of CoFe PBA (black) and Sn-CoFe PBA (red), respectively.

In the Fourier transform infrared (FTIR) spectra shown in Fig. S5, there is a strong peak for Co^{III}-C≡N-Fe^{II} in CoFe PBA and Sn-CoFe PBA near the 2119 cm^{-1} that can be attributed to the stretching vibrations of C≡N.[2,3] As can be seen, Sn-CoFe PBA has a unintended new peak at 2160 cm^{-1} for Co^{II}-C≡N-Fe^{III}.[4] Additionally, a weak peak at about 1385 cm^{-1} is correlated to C-N groups,[5] illustrating a little existence of Co-C-N-Fe. Apart from that, the peaks in two PBA framework at around 1610 cm^{-1}, 3400 cm^{-1} and 3630 cm^{-1} could be assigned to H-O-H bending vibration, O-H stretching vibration of free water and bound water,[2,3] implying the existence of trisodium citrate dehydrate.

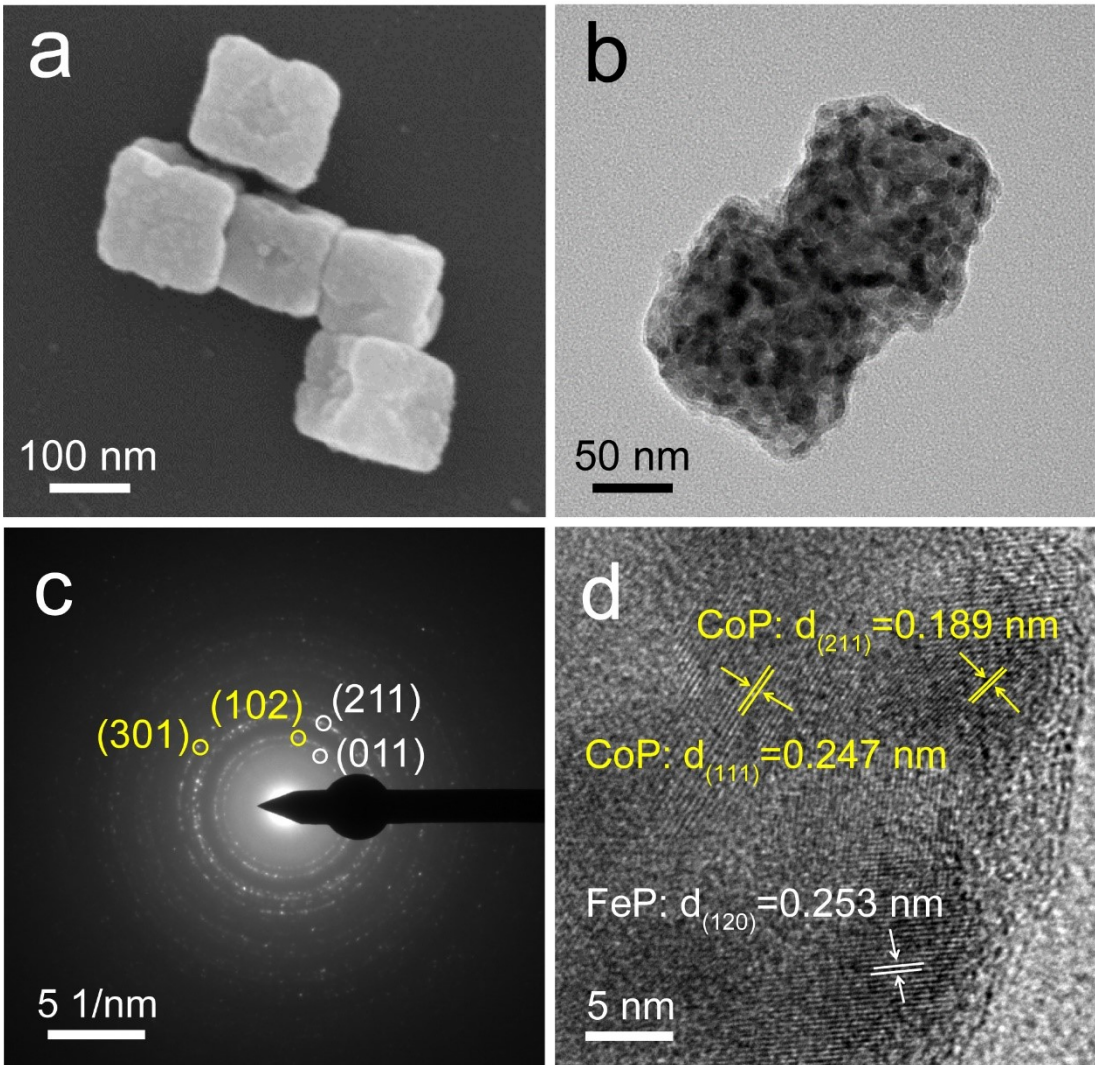

Fig. S6. (a) SEM, (b) TEM, (c) HRTEM and (d) SAED images of CoP/FeP.

The morphologies and structures of CoFe PBA and Sn-CoFe PBA after phosphating was further discussed. CoP/FeP particles were characterized by SEM (Fig. S6a), having a similar structure with CoFe PBA and retaining well of the nanocubic morphologies. Whereas, the rough surface had been observed by TEM (Fig. S6b) distinctly and further confirmed that CoP/FeP was made up of nanoparticles in the shape of cubes. The SAED images of the CoP/FeP samples are presented in Fig. S6c, the diffraction points of CoP corresponding to the (301) and (102). Moreover, (011) and (211) crystal planes match well with the FeP. As evidenced by HRTEM (Fig. S6d),

the rough nanocubes of CoP exposed to the (111) and (211) facets with the clear crystal lattice fringes spacing of 0.247 nm and 0.189nm, respectively. Besides, the FeP crystal lattice fringe spacing of 0.253 nm belong to the (120) facet.

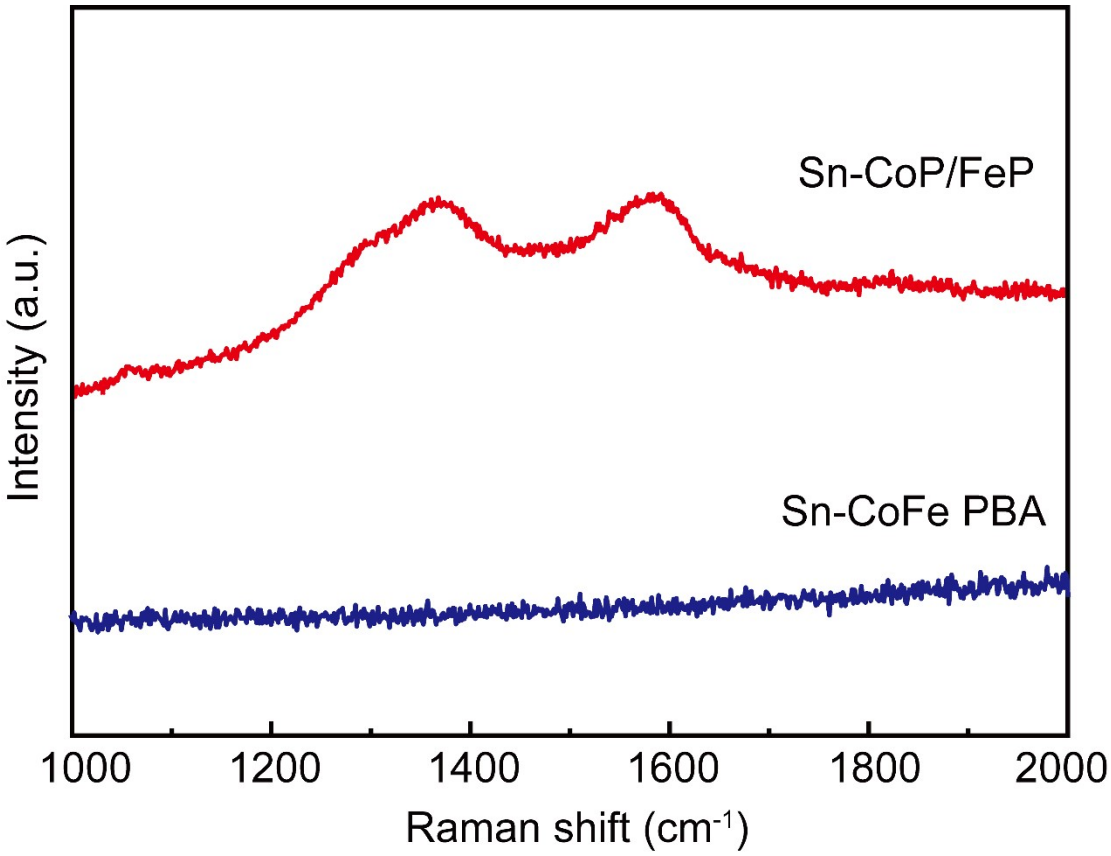

Figure S7. Raman spectra of Sn-CoFe PBA (blue) and Sn-CoP/FeP (red).

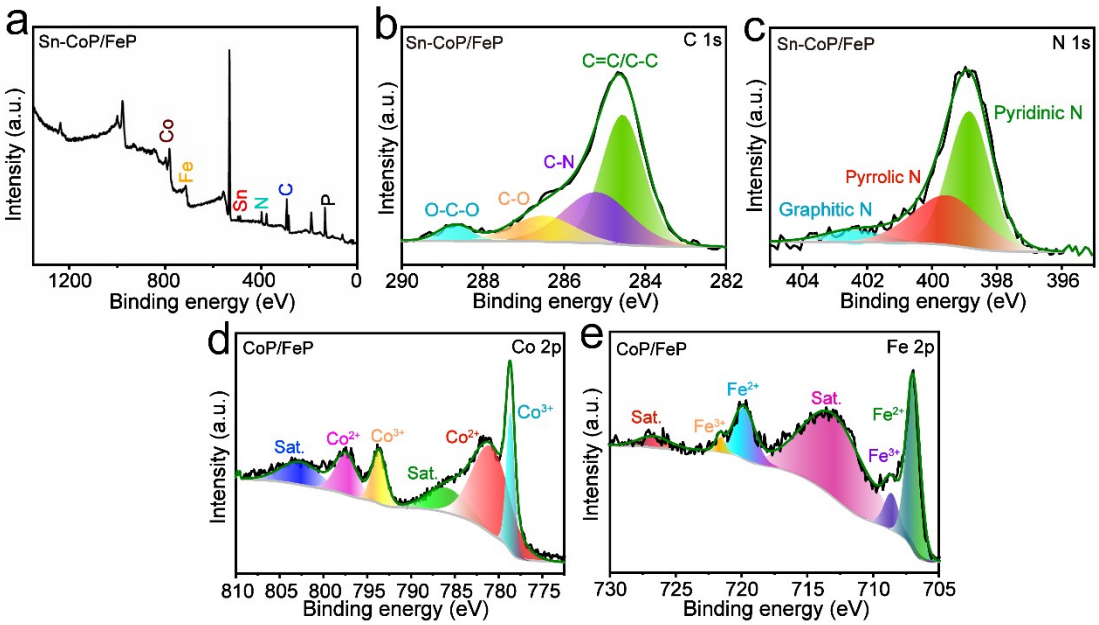

Fig. S8. (a) XPS patterns of Sn-CoP/FeP survey, (b) C 1s and (c) N 1s XPS for Sn-CoP/FeP and (d) Co 2p and (e) Fe 2p XPS for CoP/FeP.

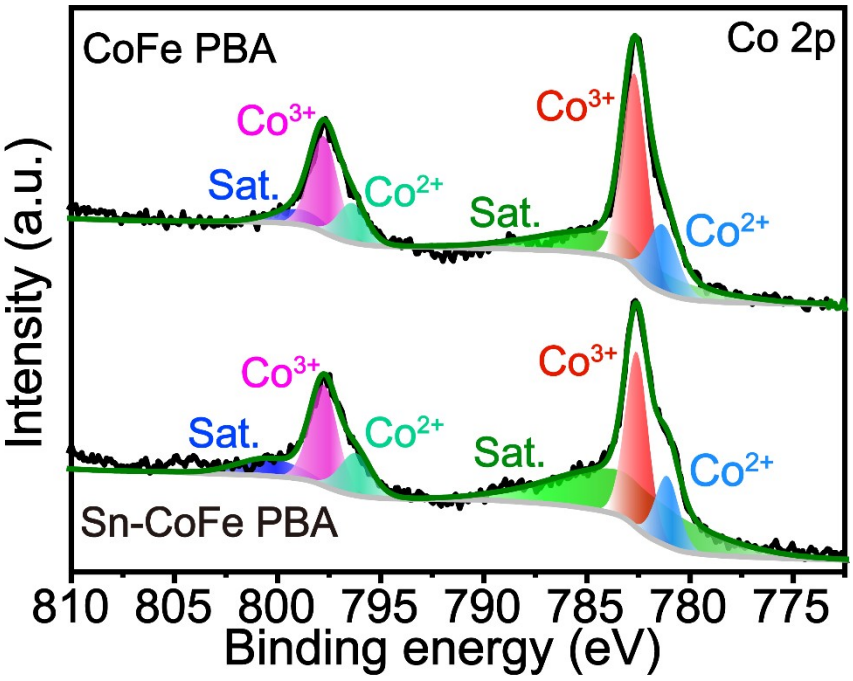

Figure S9. High-resolution XPS spectra of Co 2p of CoFe PBA and Sn-CoFe PBA.

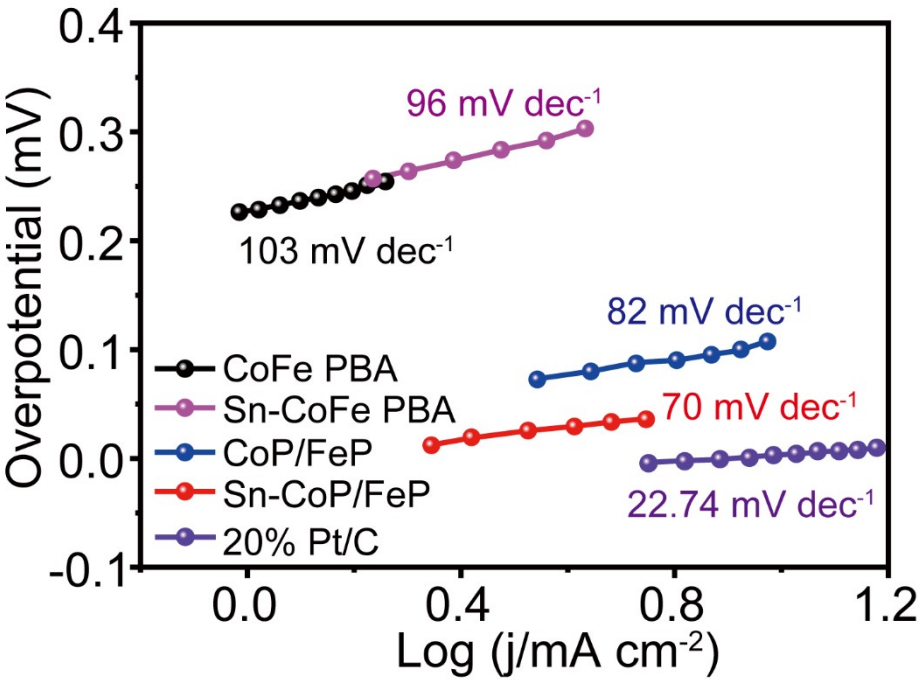

Figure S10. The steady-state Tafel slopes of 20% Pt/C, Sn-CoP/FeP, CoP/FeP, Sn-CoFe PBA and CoFe PBA using long term i-t measurement tested in 1 M KOH.

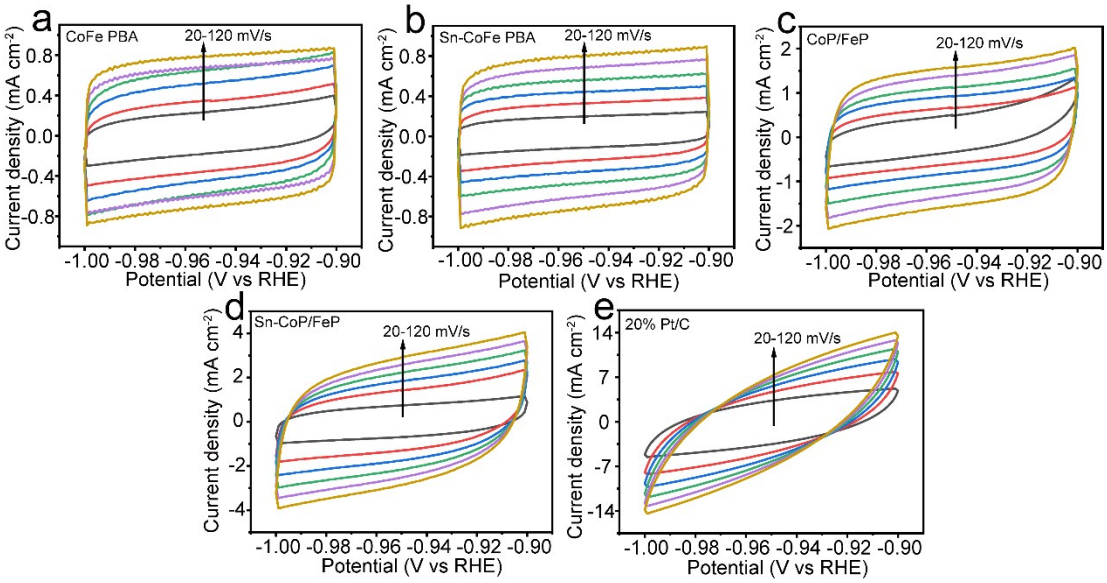

Figure S11. CV curves of (a) CoFe PBA, (b) Sn-CoFe PBA, (c) CoP/FeP, (d) Sn-CoP/FeP and (e) 20% Pt/C with different scan rate from 20 to 120 mV s^{-1} in 1 M KOH.

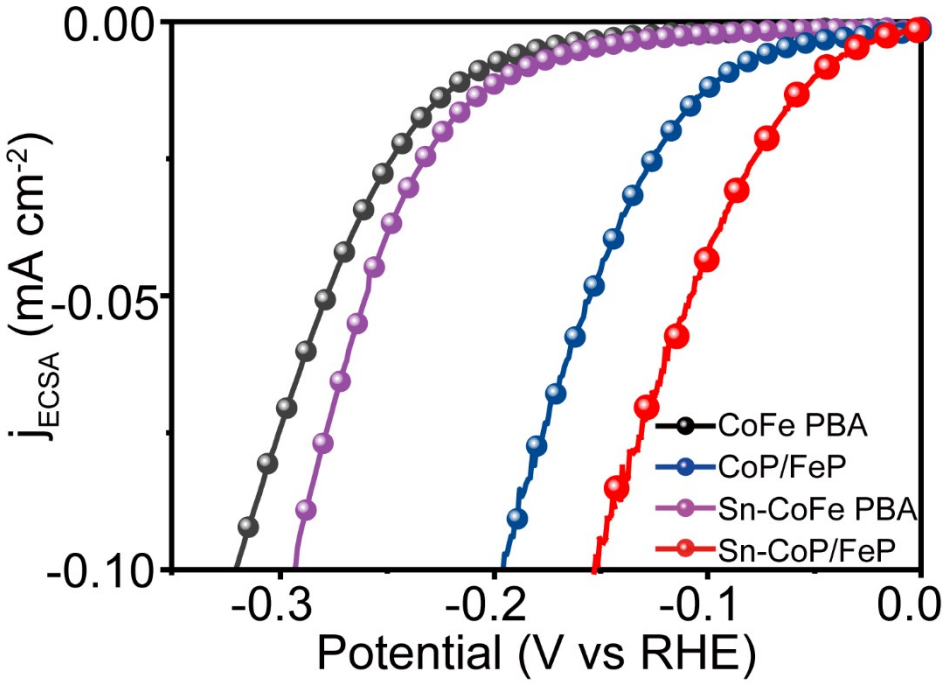

Figure S12. The ECSA-normalized LSV curves of 20% Pt/C, Sn-CoP/FeP, CoP/FeP, Sn-CoFe PBA and CoFe PBA measured in 1 M KOH for HER performance.

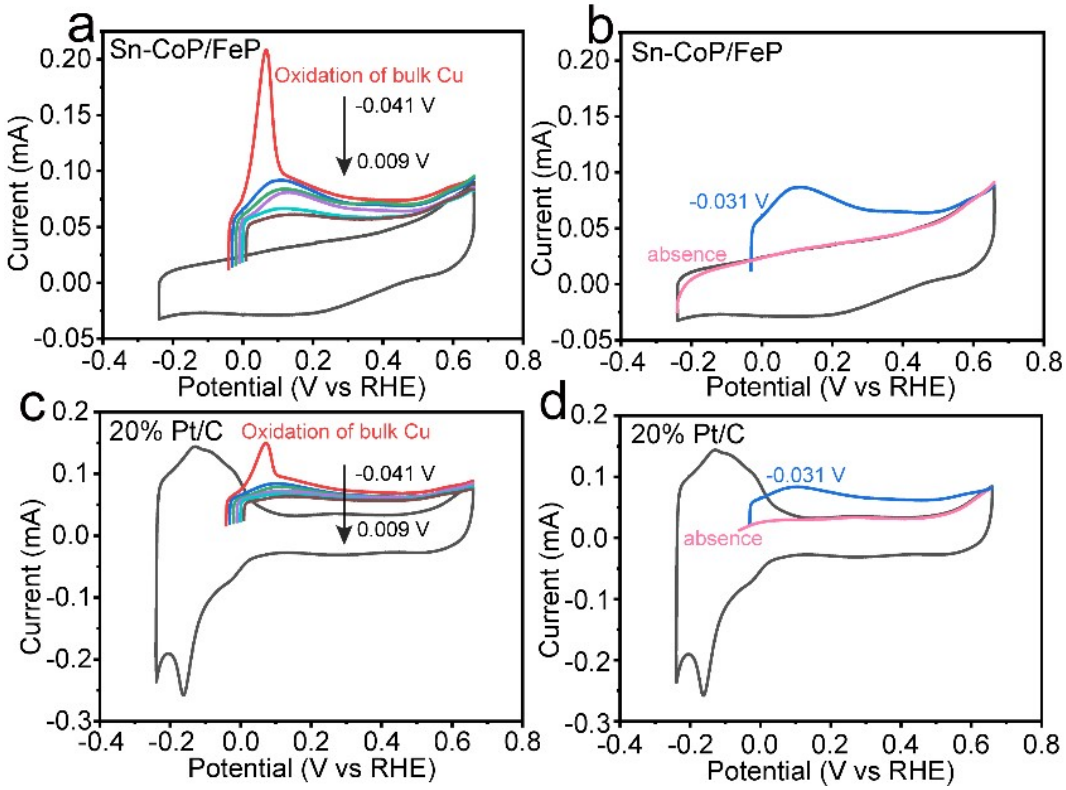

Figure S13. Copper UPD curves in 0.5 aq. M H_2SO_4 in the absence of 5 mM $CuSO_4$ on (a) Sn-CoP/FeP and (c) 20% Pt/C. The electrode was polarized at -0.041, -0.031, -0.021, -0.011, -0.001 and 0.009 V for 100 s with a scan rate of 1 mV s^{-1}. Copper UPD curves in 0.5 aq. M H_2SO_4 in the absence of 5 mM $CuSO_4$ on (b) Sn-CoP/FeP and (d) 20% Pt/C. The electrode was polarized at -0.031 V for 100 s to form UPD layer.

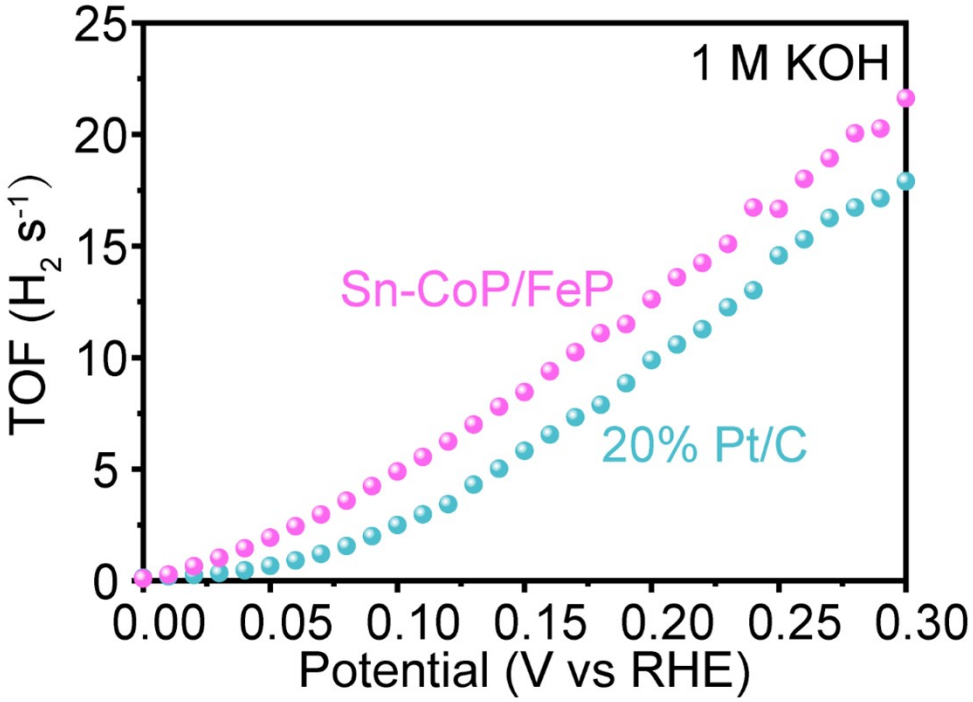

Figure S14. The relationship between TOF and the tested potential for the Sn-CoP/FeP and 20% Pt/C in 1 M KOH.

Active site measurement:

The active site was assessed by the underpotential deposition of copper (Cu-UPD) method, which has been widely used for determine the corresponding active sites.[5,6] In this manner, the number of active site (n) can be obtained by the UPD copper stripping charge (Q_{Cu}, $Cu_{UPD} \rightarrow Cu^{2+} + 2e^-$) with the following equation:

$n = Q_{Cu} / 2F$

where F is the Faraday constant (96485 C mol^{-1}).

Calculation of the turnover frequency (TOF):

The TOF (s^{-1}) can be estimated by the following equation:[7]

$TOF = I / (2nF)$

Where I is the current (A) during the linear scaning process, F is the Faraday constant (96485 C mol^{-1}), n is the number of active sits (mol). The factor 1/2 are based on the consideration that two electrons transfered to form one hydrogen molecule in the HER process.

The TOF of the as-synthesized samples were measured at 1 M KOH. It can be inferred from Figure S12 that the number of active sites of Sn-CoP/FeP and 20% Pt/C is $3.74*10^{-6}$ mol and $3.12*10^{-6}$ mol, respectively. The TOF value of Sn-CoP/FeP and 20% Pt/C is 12.62 and 9.89 s^{-1} at the potential of 200 mV, respectively, implying that the Sn-CoP/FeP possess the optimal activity.

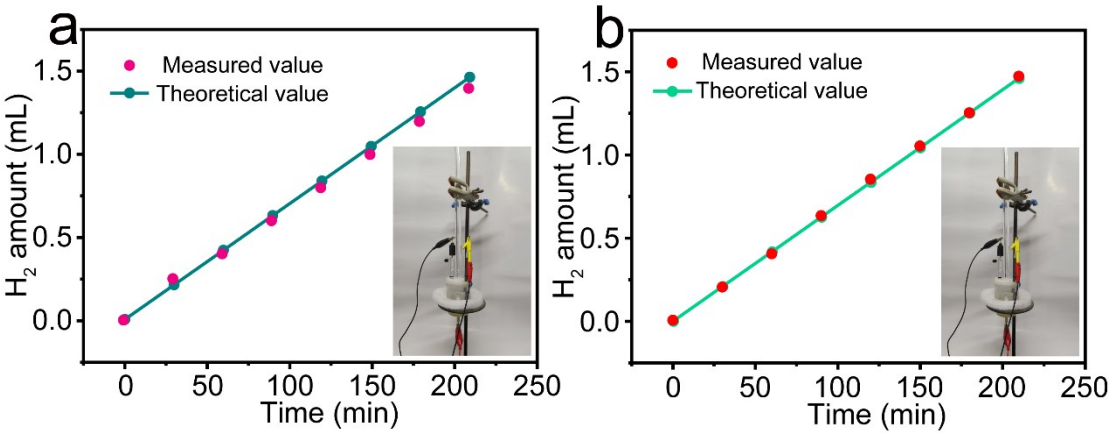

Figure S15. Faradic efficiency for hydrogen evolution of (a) CoP/FeP and (b) Sn-CoP/FeP at a current density of 10 mA cm^{-2} tested for 210 min in 1 M KOH.

The Faradic efficiency ($\Phi_{eff.}$) of gas evolution was carried out using the water drainage method. The hydrogen gas amount was calculated using the Faradic law (Equation (1)) and ideal gas equation (Equation (2)) assuming two electron was transferred to produce one H_2 molecule:

$$n \text{ (theo.)} = Q / 2F \quad (1)$$

$$n \text{ (exp.)} = PV / RT \quad (2)$$

where the total amount of charge Q (C) can be obtained by $Q = I \times t$. Then the Faradic efficiency can be expressed as:

$$\Phi_{eff.} = n \text{ (exp.)} / n \text{ (theo.)} = 2FPV / RTIt \quad (3)$$

where F is the Faradic constant (96485 C mol^{-1}), P is the standard atmospheric pressure (101325 Pa), V is the gas volume (m^3), R is the ideal gas constant (8.314 J mol^{-1} K^{-1}), T is the temperature (K), I is the current passed the electrode, and t is the electrolysis time.

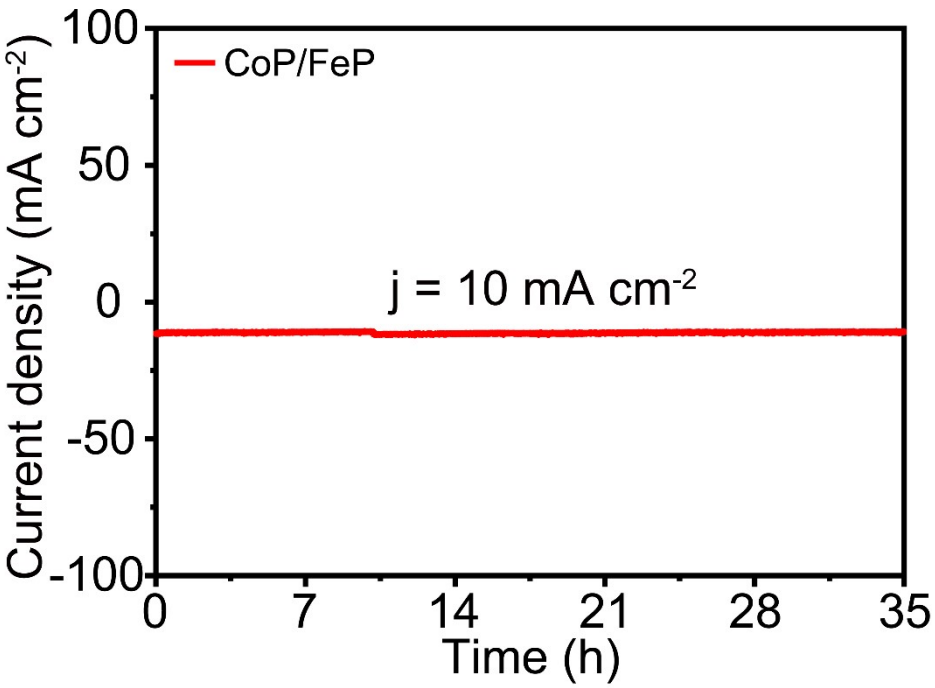

Figure S16. Long-term chronoamperometric test of CoP/FeP in 1 M KOH at current density of 10 mA cm^{-2}.

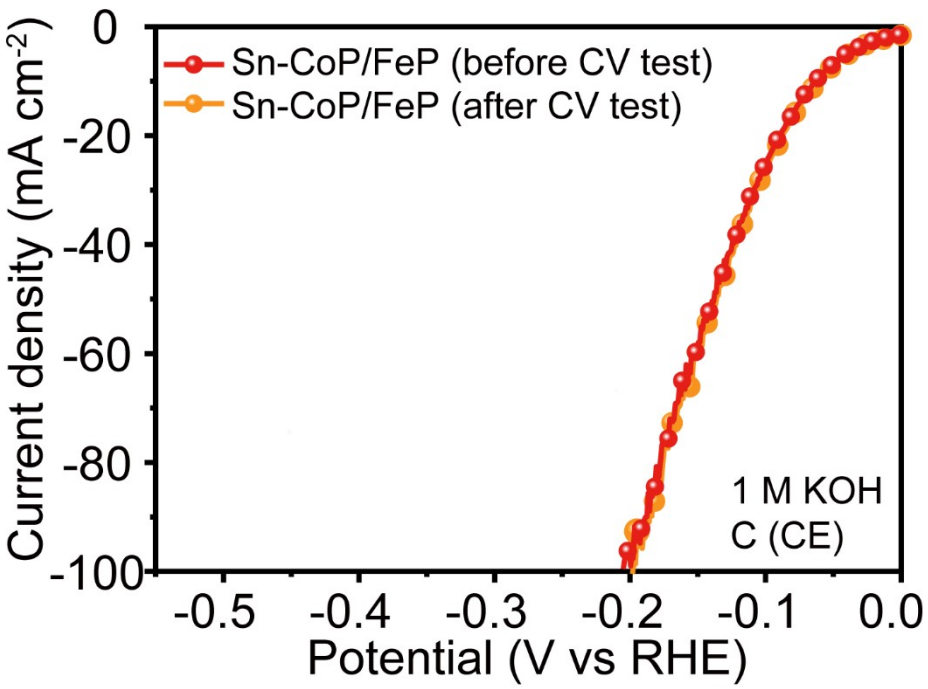

Figure S17. LSV curves of Sn-CoP/FeP after CV surveys by use of carbon rod as counter electrode in 1 M KOH.

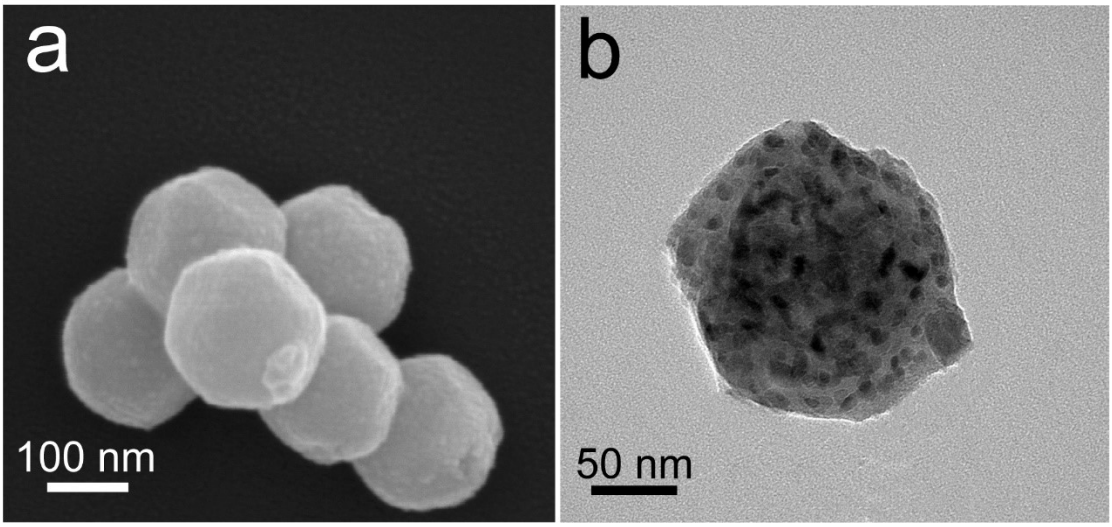

Figure S18. (a) SEM and (b) TEM images of Sn-CoP/FeP after long-term i-t measurement.

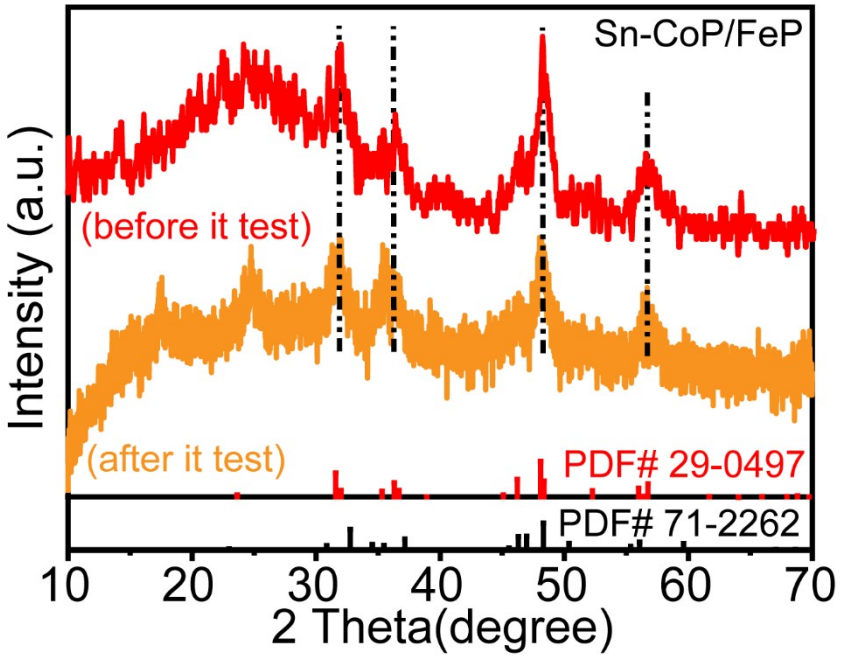

Figure S19. XRD patterns of Sn-CoP/FeP before and after long-term i-t measurement.

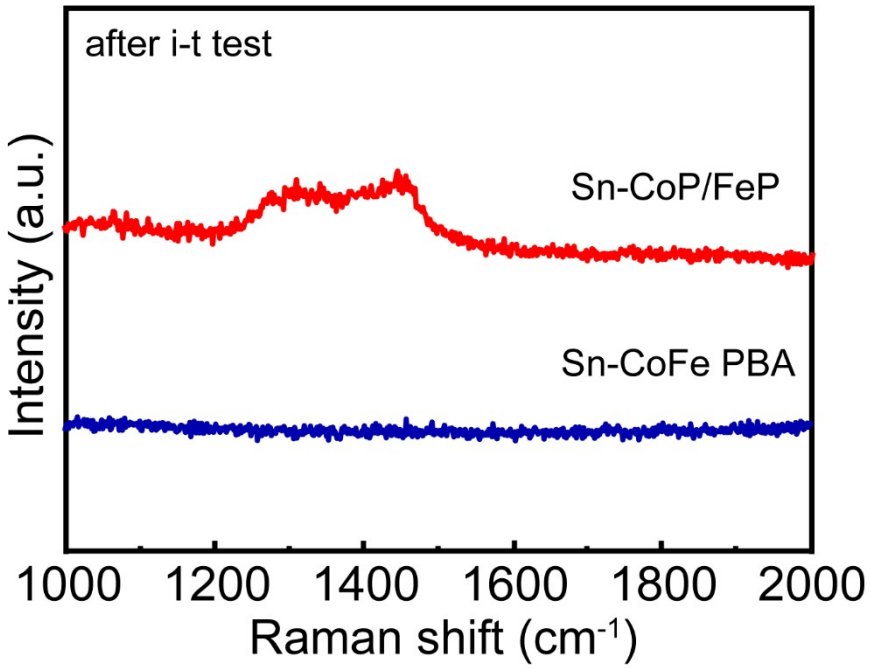

Figure S20. Raman spectra of Sn-CoFe PBA (blue) and Sn-CoP/FeP (red) after long-term i-t measurement.

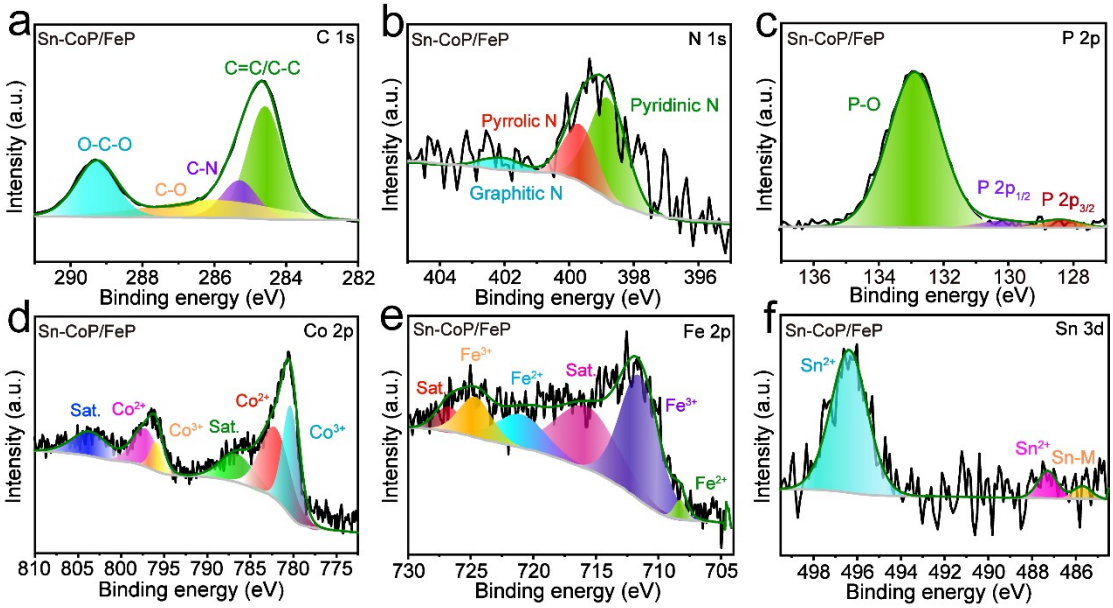

Figure S21. High-resolution XPS spectra of (a) C 1s, (b) N 1s, (c) P 2p, (d) Co 2p, (e) Fe 2p and (f) Sn 3d of Sn-CoP/FeP after long term electrochemical test.

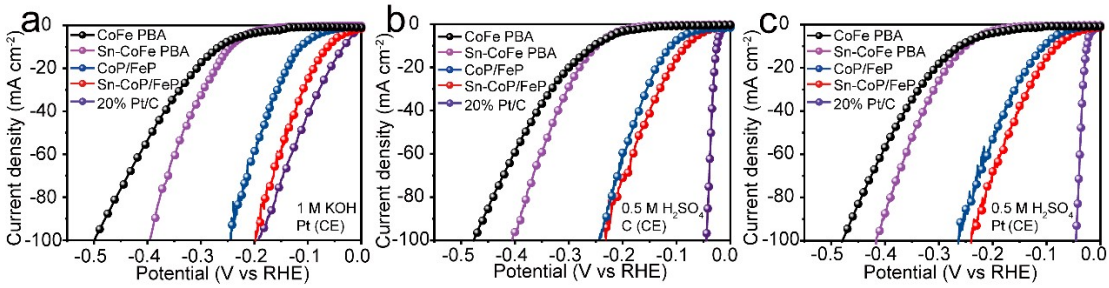

Figure S22. LSV curves of 20% Pt/C, Sn-CoP/FeP, CoP/FeP, Sn-CoFe PBA and CoFe PBA with different counter electrode by use of carbon rod and Pt plate measured in 1 M KOH and 0.5 M H_2SO_4. (a) 1 M KOH with Pt plate as counter electrode, (b) 0.5 M H_2SO_4 with carbon rod as counter electrode and (c) 0.5 M H_2SO_4 with Pt plate as counter electrode.

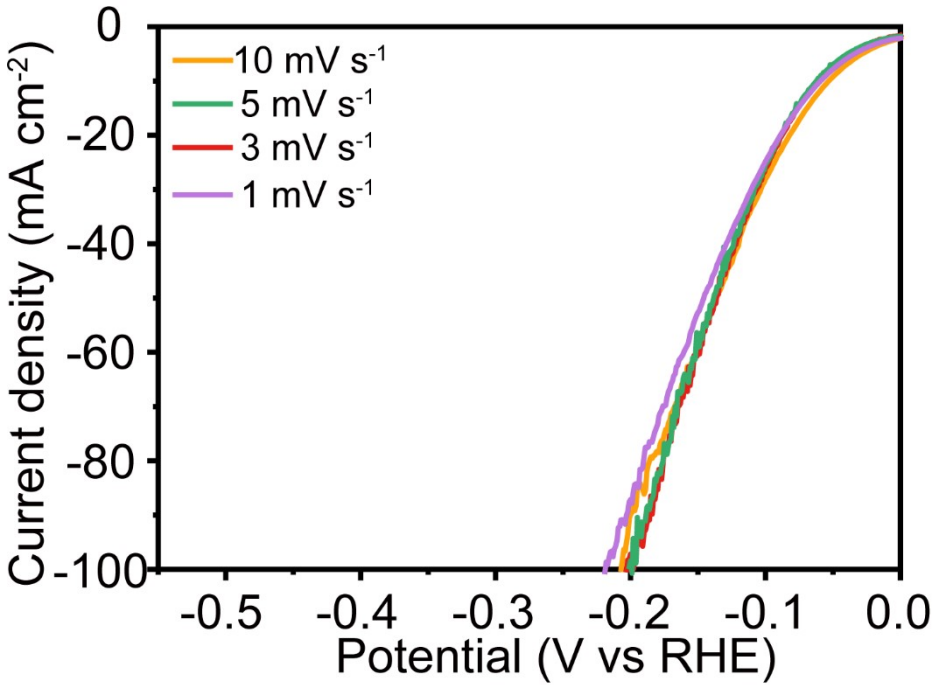

Figure S23. LSV curves of Sn-CoP/FeP with different sweep speeds of 10 mV s^{-1}, 5 mV s^{-1}, 3 mV s^{-1} and 1 mV s^{-1} by use of carbon rod measured in 1 M KOH.

Table S1. HER performance of 20% Pt/C, Sn-CoP/FeP, CoP/FeP, Sn-CoFe PBA and CoFe PBA with different counter electrode by use of carbon rod and Pt plate measured in 1 M KOH and 0.5 M H_2SO_4.

Sample	1 M KOH		0.5 M H_2SO_4	
	C (CE)/mV	Pt (CE)/mV	C (CE)/mV	Pt (CE)/mV
20% Pt/C	33	33	24	24
Sn-CoP/FeP	62	62	82	82
CoP/FeP	111	112	103	104
Sn-CoFe PBA	245	245	250	251
CoFe PBA	266	266	259	260

Table S2. The HER performance of Sn-CoP/FeP compared with other recently-reported electrocatalysts in 1 M KOH.

No.	Catalyst	η_{10} (mV)	Tafel slope (mV dec^{-1})	reference
1	Sn-CoP/FeP	62	71	This work
2	PW-Co_3N NWA/NF	41	40	Nat. Commun. 2020, 11, 1853.
3	Sn_4P_3/Co_2P SCNAs	45.4	72.8	Appl. Catal. B, 2022, 304, 120923.
4	$(Fe,Ni)_3P$/NiCoP	52.3	79.8	Chem. Eng. J. 2022, 430, 132699.
5	Co-P@IC/(Co-Fe)P@CC	53	88	Chem. Eng. J. 2021, 405, 127002.
6	A-MoP@PC	67	40	Nano-Micro Lett. 2021, 13, 215.
7	Cr-CoP/CP	67	31	Chem. Eng. J. 2021, 425, 130651.
8	NiMoP/NF	68	87	Appl. Catal. B, 2021, 297, 120434.
9	Co-Fe-P/CeO_2 HHRs	69.7	90.1	Chem. Eng. J. 2022, 437, 135376.
10	WN-Ni@N,P-CNT-800	70	151.7	Appl. Catal. B, 2021, 298, 120511.
11	MoP-MoS_2/HCSs	71	47.68	Chem. Eng. J. 2022, 438, 135544.
12	Co-Ni_xP_y@Co_3O_4/NF	72	56.26	Chem. Eng. J. 2021, 422, 130062.
13	P-NiS_2-500	73	86.51	Chem. Eng. J. 2021, 420, 127630.
14	NiCoZnP/NC	74	47.51	Chem. Eng. J. 2021, 422, 130533.
15	Co_xP-Fe_2P/NF	75	90.26	ACS Sustainable Chem. Eng. 2021, 9, 7737-7748.
16	$Co_{0.31}Mo_{1.69}C$/MXene/NC	75	32	ACS Nano 2020, 14, 10834-10864.
17	Fe-CoP/NF	78	92	Adv. Sci. 2018, 5, 1800949.
18	Mo-CoP/NC/TF	78	48.1	Chem. Eng. J. 2021, 405, 126981.
19	MoP/MoO_2	79	41	Chem. Eng. J. 2022, 430,

				132674.
20	P-CoFe-LDH@MXene/NF	85	98.59	Appl. Catal. B, 2021, 299, 120660.
21	P-WS_2	88	62	Nano Res. 2022, 15, 4, 2855-2861.
22	Ni-CoP-5%	88	41	Nano Lett. 2021, 21, 823-832.
23	FeCo-FeCoP@C@NCCs	91	58	J. Energy Chem. 2021, 53, 1-8.
24	Ni_2P-Co_2P/CC	93	65	Chem. Eng. J. 2021, 424, 130444.
25	Co-VO_x-P	98	59	Appl. Catal. B, 2022, 304, 120985.
26	Mo,Fe-$NiCoP_x$/NF	99	44.6	J. Colloid Interface Sci. 2022, 615, 456-464.
27	CoFe PBA@CoP/NF	100	60.8	Small Methods, 2021, 5, 2100125.
28	Ni_2P-Ru_2P/NF	101	56.7	Appl. Catal. B, 2022, 304, 120914.
29	NiFeP@NiP@NF	105	97.9	ACS Appl. Mater. Interfaces 2021, 13, 23702-23713.
30	R-Mn-CoP@Mn-CoOOH	110	45	Appl. Catal. B 2021, 292, 120172.
31	Fe-Co-O/Co@NC-mNS/NF	112	96	Small 2021, 17, 2101312.
32	CoFeP NS@NCNF	113	108	J. Colloid Interface Sci. 2021, 602, 619-626.
33	$Fe_xCo_{2-x}P$/NF	114	97	ChemSusChem 2019, 12, 4810-4823.
34	FNP	116	68	Chem. Eng. J. 2020, 390, 124515.
35	Ni-CoP/Co_2P@NC	117	68	Chem. Eng. J. 2022, 433, 133523.
36	Co_2P/CoP@Co@NCNT	118	46	Chem. Eng. J. 2022, 430, 132877.
37	NHPBAP	121	67	Adv. Energy Mater. 2018, 8, 1800484.
38	NiF_3/Ni_2P@CC-2	121	75	Chem. Eng. J. 2022, 427, 130865.
39	p-NFNR@Ni-Co-P	125	85	ACS Appl. Mater. Interfaces 2021, 13, 48949-48961.
40	NiFeP/CC	129	76.8	Chem. Eng. J. 2021, 420, 129972.

41	$Co_{0.6}Fe_{0.4}P$-1.125	133	61	Chem.Sci. 2019, 10, 464-474.
42	Cu_3P-Cu_2O/NPC	138	62.64	Chem. Eng. J. 2022, 427, 130946.
43	CoP@FeCoP/NC	141	56.34	Chem. Eng. J. 2021, 403, 126312.
44	D-CoNiO_x-P-NFs	145	76	Energy Environ. Sci. 2020, 13, 5097-5103.
45	CFP NFs@NPGA	155	67.2	J. Power Sources, 2020, 456, 228015.
46	NiCoN|Ni_xP|NiCoN	165	139.2	ACS Energy Lett. 2020, 5, 2681-2689.
47	DLD-FeCoP@CNT	166	57.1	J. Mater. Sci. Technol. 2021, 74, 11-20.
48	CoP@3D Ti_3C_2-MXene	168	58	ACS Nano, 2018, 12, 8017-8028.
49	FeNiP/PG	173	50.3	J. Mater. Chem. A, 2019, 7, 14526-14535.
50	FeP/HCNB	180	71	Carbon, 2019, 152, 16-23.
51	CuCoSe@HCNF	181	59	Appl. Catal. B, 2021,293,120209.
52	NCT@CoP@MoS_2	195	74	Chem. Eng. J. 2021, 419, 129977.
53	Fe-Ni_5P_4/NiFeOH-350	197	94	Appl. Catal. B, 2021, 291, 119987.

Reference

1 J. Shi, F. Qiu, W. Yuan, M. Guo and Z.-H. Lu, Nitrogen-Noped Carbon-Decorated Yolk-Shell CoP@FeCoP Micro-Polyhedra Derived from MOF for Efficient Overall Water Splitting. *Chem. Eng. J.,* 2021, **403**, 126312.

2 J. Li, L. He, J. Jiang, Z. Xu, M. Liu, X. Liu, H. Tong, Z. Liu and D. Qian, Facile Syntheses of Bimetallic Prussian Blue Analogues ($K_xM[Fe(CN)_6]\cdot nH_2O$, M=Ni, Co, and Mn) for Electrochemical Determination of Toxic 2-Nitrophenol. *Electrochim. Acta,* 2020, **353**, 136579.

3 M. Hafezi Kahnamouei and S. Shahrokhian, Mesoporous Nanostructured Composite Derived from Thermal Treatment CoFe Prussian Blue Analogue Cages and Electrodeposited NiCo-S as an Efficient Electrocatalyst for an Oxygen Evolution Reaction. *ACS Appl. Mater. Interfaces,* 2020, **12**, 16250-16263.

4 A. Bordage, R. Moulin, E. Fonda, G. Fornasieri, E. Riviere and A. Bleuzen, Evidence of the Core-Shell Structure of (Photo)magnetic CoFe Prussian Blue Analogue Nanoparticles and Peculiar Behavior of the Surface Species. *J. Am. Chem. Soc.,* 2018, **140**, 10332-10343.

5 L. Zeng, L. Xiao, X. Shi, M. Wei, J. Cao, and Y. Long, Core-Shell Prussian Blue Analogues@ Poly(m-phenylenediamine) as Efficient Peroxymonosulfate Activators for Degradation of Rhodamine B with Reduced Metal Leaching. *J. Colloid Interface Sci.,* 2019, **534**, 586-594.

6 D. H. Kweon, M. S. Okyay, S.-J. Kim, J.-P. Jeon, H.-J. Noh, N. Park, J. Mahmood and J.-B. Baek, Ruthenium Anchored on Carbon Nanotube Electrocatalyst for Hydrogen Production with Enhanced Faradaic Efficiency, *Nat. Commun.,* 2020, **11**, 1278.

7 J. Mahmood, F. Li, S.-M. Jung, M. S. Okyay, I. Ahmad, S.-J. Kim, N. Park, H. Y. Jeong and J.-B. Baek, An Efficient and pH-Universal Ruthenium-Based Catalyst for

the Hydrogen Evolution Reaction, *Nat. Nanotech.,* 2017, **12**, 441-446.